Thermal boundary-layer solutions for forced convection in a porous domain above a flat plate

Miltiadis V. Papalexandris[1]

[1]Institute of Mechanics, Materials and Civil Engineering, Université catholique de Louvain, Louvain-la-Neuve 1348, Belgium.

Contributing authors: miltos.uclouvain.be;

Abstract

In this paper we present numerical solutions for thermal boundary layers that are developed during forced convection in a porous medium located above a flat plate. The basic feature of such layers is that they are nonsimilar. In our study we consider thermal nonequilibrium between the two phases. Accordingly, each phase is endowed with its own energy equation. The boundary-layer equations are solved with the local nonsimilarity method. We examine convection of air and liquid water, while the solid matrix is supposed to be made of cast iron. According to our computations, there are significant differences between the temperature distributions of the two phases, especially at short and moderate distances from the edge of the flat plate. Also, due to the high conductivity of the solid matrix, the thermal boundary layers are much thicker than the hydrodynamic one. The profile of the local Nusselt number is quite sensitive on the Prandtl number and only far downstream it scales with the square root of the distance. Finally, the validity of the local thermal equilibrium assumption is assessed via a comparative study. According to it, this assumption leads to significant inaccuracies in the temperature profiles but yields reasonable estimates for the thickness of the thermal boundary layer of the fluid.

Keywords: nonsimilar boundary layers, porous media, local nonsimilarity method, thermal nonequilibrium, Darcy-Forchheimer law.

MSC Classification: 76D10 , 76S05 , 76M45

1 Introduction

Forced convection in porous media is encountered in numerous natural processes and technological applications. Examples of relevant natural phenomena are wind through vegetation canopies and urban areas, water flow in coral reefs and emergent vegetation, solidification of multi-component melts, and many others. Technological applications include heat-transfer equipment, filtration systems, fuel cells etc. The literature on this field is vast and the interested reader is referred to textbooks such as [1–4] and references therein.

In this paper we derive and discuss thermal boundary-layer solutions of forced convection in a highly porous domain situated above a flat plate. The main feature of such layers is that they are nonsimilar, which implies that the boundary-layer equations cannot be reduced to Ordinary Differential Equations (ODEs). This is due to the presence of a characteristic length scale in the flow of interest, namely, the representative size of the fibers that comprise the solid matrix of the porous medium.

Even though porous-media flows have been the subject of intense research over the years, relatively few studies focused on boundary layers at the interface of a porous medium and an impermeable solid boundary. One of the earliest works on this topic was that of Vafai & Tien [5]. Later, numerical solutions for the flow of interest were provided in [6, 7]. In [6] the velocity profile was given in terms of an asymptotic power-series of the porosity, while in [7] it was computed analytically via quadrature of the boundary-layer momentum equation. However, in those earlier studies, the (nonlinear) advective term of the momentum equation was not taken into account.

Subsequently, Nakayama et al. [8] considered the full boundary-layer momentum equation (including the advective term) and presented numerical solutions for the hydrodynamic and thermal boundary layers by employing the local similarity solution method [9]. According to this method, at any given streamwise location, the flow is approximated as self-similar and, therefore, the governing equations are reduced to a set of location-specific ODEs. Also, Hossain et al. [10] provided numerical solutions for boundary-layer flows around a wedge embedded in a porous medium. While Celli et al. [11] studied the structure of the thermal layers of interest but assumed constant velocity profile, i.e. absence of a hydrodynamic boundary layer. Very recently, the authors of [12] employed the Chebyshev collocation method to obtain numerical solutions for forced convection above a flat plate embedded in an infinite porous medium by assuming a purely Darcian interphasial drag and an ad hoc freestream velocity profile. Finally, a number of recent studies [13–15] were devoted to the boundary layers of Casson fluid (which is shear-thinning) in a porous medium.

However, in all of the aforementioned works it was assumed that the solid impermeable boundary (the flat plate) was embedded in a porous medium that covered the entire plane. This means that the porous medium did not start at the edge of the solid boundary but, instead, covered the space upstream of the flat plate as well. An important simplification afforded by this setup is that

the free-stream velocity (i.e. the velocity outside the boundary layer) is constant, which in turn reduces considerably the complexity of the boundary-layer equations. Additionally, all of the aforementioned studies, with the exception of [11, 12], were based on the assumption of the Local Thermal Equilibrium (LTE) between the solid matrix and the fluid. This assumption implies that the difference between the temperatures of the two phases is very small everywhere and can thus be neglected.

Recently, we derived boundary-layer solutions for isothermal forced flow of a Newtonian fluid in a porous medium located above a flat plate [16]. Therein, in contrast to earlier works, the porous medium covers only the quarter-plane above the flat plate and does not extend to the space upstream of it; see also figure 1 below. Accordingly, the free-stream velocity in the porous medium is no longer constant but varies with the streamwise distance, i.e. the horizontal distance from the edge of the flat plate. In [16] the boundary layer equations are solved with the local nonsimilarity method [9, 17] which is a potent and popular approach for the numerical treatment of nonsimilar boundary layers.

In the present paper, we extend upon our earlier work [16] and present boundary-layer solutions for convective heat transfer of a Newtonian fluid in a porous medium. More specifically, the temperature of the incoming stream right ahead of the porous medium is different than the temperature of the flat plate above which the porous medium is located. Since the hydrodynamic boundary layers for the problem in hand were studied in [16], herein we focus on the structure of the thermal boundary layers. Numerical results are provided for air at $Pr = 0.73$ and liquid water at $Pr = 7$. Our analysis focuses on the evolution of the temperature profiles, the boundary layer thickness and the variation of the local Nusselt number. To the author's knowledge, detailed experimental data for this setup are currently unavailable. In our study we take into account thermal nonequilibrium between the two phases, i.e. we do not invoke the LTE assumption. Accordingly, each phase is endowed with its own energy equation. Additionally, in a separate section we provide an assessment on the validity of this assumption for the problem in hand by comparing numerical predictions made with and without it.

The paper is structured as follows. In section 2, we present the mathematical model of the problem. In section 3 we elaborate on the free-stream velocity inside the porous medium. In section 4 we derive the boundary-layer equations, and in section 5, we present the algorithm for their numerical solution which is also based on the local nonsimilarity method. In section 6 we present our numerical results while in section 7 we assess the validity of the LTE assumption. Finally, section 8 concludes.

2 Problem statement and mathematical model

In terms of notation, symbols with a hat $\hat{\cdot}$ stand for dimensional variables, while symbols without a hat denote dimensionless ones. Let us consider a porous medium of constant porosity ϕ covering completely the quarter-plane

defined by $\hat{x} > 0$ and $\hat{y} > 0$. A flat, solid and impermeable plate is located just below the porous medium at $\hat{y} = 0$. We also consider an incoming stream of fluid parallel to the flat plate at $\hat{x} = 0$. Right ahead of the porous medium, the fluid stream has uniform velocity $\hat{u}_0$ and temperature $\hat{T}_0$. Whereas the flat plate is maintained at a uniform temperature $\hat{T}_\mathrm{w}$ which is different than $\hat{T}_0$. The schematic representation of the problem in hand is provided in figure 1. It is important to note that, independent of the value of $\hat{u}_0$, the flow inside the porous medium can be sustained only by applying an external forcing; otherwise the resistance of the solid matrix of the porous medium would eventually reduce the fluid velocity to zero.

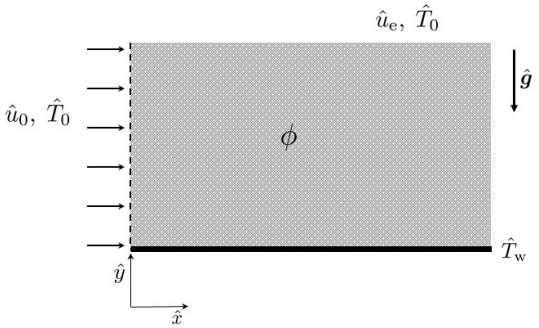


Fig. 1 Schematic representation of the physical problem.

The boundary-layer equations of our study are derived from the thermo-mechanical model of [18] for flows in domains partially or fully covered by porous media. This model is based on a mixture-theoretic formalism and has been used in several of our studies on porous-media flows [19–22]. According to this formalism, the solid matrix and the fluid phase are considered to be two distinct, coexisting but immiscible thermodynamic continua [2, 23]. Each phase is endowed with its own set of kinematic and thermodynamic variables and balance laws. Then, the porosity ϕ is introduced as a concentration variable that provides, at each point in space, the volume fraction of the fluid. Accordingly, it is bounded between zero and unity, $0 < \phi \leq 1$.

The solid matrix of the porous medium is assumed to be comprised of rigid, non-reacting fibers at rest. Therefore, its mass and momentum-balance equations are trivially satisfied. The flow inside the porous medium is steady and at low Mach number. Under these assumptions, the mass, momentum and energy-balance laws of the fluid phase [18] reduce to,

$$\nabla \cdot (\hat{\rho}\phi\hat{\boldsymbol{u}}) = 0\,, \tag{1}$$

$$\nabla \cdot (\hat{\rho}\phi\hat{\boldsymbol{u}}\hat{\boldsymbol{u}}) + \phi\nabla\hat{p} = \nabla \cdot \left(\hat{\mu}\phi\hat{\boldsymbol{V}}^\mathrm{d}\right) - \hat{\boldsymbol{\delta}}\cdot\hat{\boldsymbol{u}} + \hat{\rho}\phi\hat{\boldsymbol{g}}\,, \tag{2}$$

$$\phi\hat{\rho}\hat{c}_p\hat{\boldsymbol{u}} \cdot \nabla\hat{T} = \nabla \cdot \left(\phi\hat{\kappa}\nabla\hat{T}\right) + \hat{h}\left(\hat{T} - \hat{T}_\mathrm{s}\right)\,. \tag{3}$$

The steady-state form of the energy-balance law for the solid matrix reads,

$$\nabla \cdot \left((1-\phi) \hat{\boldsymbol{\kappa}}_{\mathrm{s}} \nabla \hat{T}_{\mathrm{s}} \right) - \hat{h} \left(\hat{T} - \hat{T}_{\mathrm{s}} \right) = 0 \,. \tag{4}$$

In the above equations, $\hat{\rho}$, $\hat{T}$, $\hat{p}$ and $\hat{\boldsymbol{u}} = (\hat{u}, \hat{v})$ denote the density, temperature, dynamic pressure and velocity vector of the fluid phase, respectively. As mentioned above, the flow inside the porous medium is maintained by an external forcing $\hat{\boldsymbol{F}} = (\hat{F}, 0)$. Therefore, the pressure gradient is decomposed as follows, $\nabla \hat{p} = -\hat{\boldsymbol{F}} + \nabla \hat{p}'$. Further, $\hat{T}_{\mathrm{s}}$ stands for the temperature of the solid matrix. Also $\hat{c}_p$, $\hat{\mu}$ and $\hat{\kappa}$ are, respectively, the specific heat capacity at constant pressure, dynamic viscosity and thermal conductivity of the fluid. In equation (2), $\hat{\boldsymbol{V}}^{\mathrm{d}}$ is twice the deviatoric part of the strain-rate tensor, $\hat{\boldsymbol{V}}^{\mathrm{d}} = \nabla \hat{\boldsymbol{u}} + (\nabla \hat{\boldsymbol{u}})^{\top} - \frac{2}{3} (\nabla \cdot \hat{\boldsymbol{u}}) \boldsymbol{I}$, with $\boldsymbol{I}$ being the identity matrix. Whereas, $\hat{\boldsymbol{g}}$ is the gravitational acceleration and points to the $\hat{y}$ direction, i.e. it is normal to the flat plate and to the incoming stream.

Also, in the above equations, $\hat{\boldsymbol{\kappa}}_{\mathrm{s}}$ is the thermal-conductivity tensor of the solid matrix, $\hat{\boldsymbol{\delta}}$ is the interphasial drag-coefficient tensor and $\hat{h}$ is the interphasial heat-exchange coefficient. In general, the solid matrix is an anisotropic medium and, therefore, both $\hat{\boldsymbol{\kappa}}_{\mathrm{s}}$ and $\hat{\boldsymbol{\delta}}$ are in principle second-order tensors. The parametrization of $\hat{\boldsymbol{\delta}}$ is such that the resulting interphasial (drag) force, $\hat{\boldsymbol{\delta}} \cdot \hat{\boldsymbol{u}}$, follows the Darcy-Forchheimmer law [1].

The solid matrix is assumed to consist of a sparse array of identical circular cylinders of diameter $\hat{d}_{\mathrm{c}}$. This type of solid matrix is used in the modeling of emergent canopies [24, 25] and is also encountered in cooling devices of electronic equipment. In the present study, this particular choice of solid matrix has been made because i) it allows for the derivation of precise expressions for the interphasial drag that do not involve the empirical Forchheimer coefficient, and ii) it leads to a straightforward parametrization of the interphasial heat-exchange coefficient $\hat{h}$.

Further, these cylindrical elements are considered to be very long, thin and perpendicular to the flat plate. This implies that the solid matrix is actually an orthotropic medium and, therefore, both $\hat{\boldsymbol{\kappa}}_{\mathrm{s}}$ and $\hat{\boldsymbol{\delta}}$ are diagonal. With regard to $\hat{\boldsymbol{\kappa}}_{\mathrm{s}}$, its diagonal element in the cross-stream direction is equal to the thermal conductivity κ_{s} of the material that the solid matrix is made of. The value of its diagonal element in the streamwise direction does not enter the boundary-layer equations; nonetheless since the cylinder array is very sparse and the cylinders are very thin, one may approximate it by zero.

With regard to $\hat{\boldsymbol{\delta}}$, let $\hat{\delta}_{11}$ and $\hat{\delta}_{22}$ denote its diagonal elements. The derivation of the parametrization of the component $\hat{\delta}_{11}$ has been elaborated in [16]. Herein we outline the basic steps of the derivation. For a single cylinder in cross flow, the average drag per unit length in the horizontal $\hat{x}$ direction is given by $\hat{f}_{\mathrm{c}} = \frac{1}{2} c_{\mathrm{D}} \hat{\rho} \hat{d}_{\mathrm{c}} |\hat{u}| \hat{u}$, where c_{D} is the bulk drag coefficient for cylinder arrays. For circular cylinders, we make use of the relation in [24, 26], $c_{\mathrm{D}} = 2 \left(\frac{\alpha_0}{Re_{\mathrm{c}}} + \alpha_1 \right)$ where $Re_{\mathrm{c}} = \frac{\hat{\rho} \hat{d}_{\mathrm{c}} |\hat{u}|}{\hat{\mu}}$ is the local cylinder-based Reynolds

number. In this relation, α_0 and α_1 are constants that depend on the size of the cylindrical elements and the porosity of the medium. The authors of [25] presented correlations for these two parameters based on curve-fitting of experimental data. For sufficiently thin cylinders, these correlations reduce to $\alpha_0 = 32$ and $\alpha_1 = 0.5 + 3.2(1-\phi)$. By substituting these correlations in the expression of $\hat{f}_\mathrm{c}$ and upon multiplication with the number of cylinders per unit area, $N_\mathrm{c} = \frac{4(1-\phi)}{\pi \hat{d}_\mathrm{c}^2}$, we arrive at the following expression for $\hat{\delta}_{11}$,

$$\hat{\delta}_{11} \;=\; \frac{128}{\pi}(1-\phi)\frac{\hat{\mu}}{\hat{d}_\mathrm{c}^2} \;+\; \left(2(1-\phi) + 12.8(1-\phi)^2\right)\frac{\hat{\rho}}{\pi \hat{d}_\mathrm{c}}|\hat{u}|\,. \tag{5}$$

Under the boundary-layer assumption, the momentum equation in the cross-stream direction is automatically satisfied to the first order. Therefore, the parametrization of $\hat{\delta}_{22}$ is irrelevant to the present study; the interested reader is referred to [18] for more information on its parametrization.

A similar procedure is followed for the parametrization of the interphasial heat-transfer coefficient $\hat{h}$. More specifically, we consider the heat-transfer coefficient for a single cylinder in cross-flow, $\hat{h}_\mathrm{c} = \frac{\hat{\kappa} Nu_\mathrm{c}}{\hat{d}_\mathrm{c}}$ with Nu_c being the local cylinder-based Nusselt number. An approximation for $\hat{h}$ can then be obtained by multiplying $\hat{h}_\mathrm{c}$ with the number density per unit area N_c and with the surface area per unit length of cylinder (i.e. the perimeter of a single cylinder) $\pi \hat{d}_\mathrm{c}$. The resulting parametrization reads,

$$\hat{h} \;=\; \hat{h}_\mathrm{c}\, N_\mathrm{c}\, (\pi \hat{d}_\mathrm{c}) \;=\; \frac{4(1-\phi)}{\hat{d}_\mathrm{c}^2}\,\hat{\kappa} Nu_\mathrm{c}\,. \tag{6}$$

For the local cylinder-based Nusselt number Nu_c, we employ the following correlation [27],

$$Nu_\mathrm{c} \;=\; 0.3 + \frac{0.62\, Pr^{\frac{1}{3}}}{\left(1 + \left(\frac{0.4}{Pr}\right)^{\frac{2}{3}}\right)^{\frac{1}{4}}}\, Re_\mathrm{c}^{\frac{1}{2}}\,, \tag{7}$$

where Pr is the Prandtl number of the fluid. In fact, this correlation is the approximation of equation (7.54) in [27] for small and moderate Re_c.

For the problem in hand, we assume that the fluid density and transport properties of the two phases are constant. Also, $\hat{d}_\mathrm{c}$ and $\hat{u}_0$ are set as the reference length and velocity, respectively. Accordingly, the Reynolds number of the incoming stream based on the diameter of the elements of the solid matrix, Re_0, is given by,

$$Re_0 \;=\; \frac{\hat{\rho}\hat{u}_0\hat{d}_\mathrm{c}}{\hat{\mu}}\,. \tag{8}$$

Further, we introduce the dimensionless normalized temperatures θ and θ_s,

$$\theta \;=\; \frac{\hat{T} - \hat{T}_0}{\hat{T}_\mathrm{w} - \hat{T}_0}\,, \qquad\qquad \theta_\mathrm{s} \;=\; \frac{\hat{T}_\mathrm{s} - \hat{T}_0}{\hat{T}_\mathrm{w} - \hat{T}_0}\,. \tag{9}$$

Upon non-dimensionalization of the system of governing equations (1)–(4) and by employing standard scaling arguments [27], we arrive at the boundary-layer equations for forced convection in the porous medium of interest,

$$\frac{\partial u}{\partial x} + \frac{\partial v}{\partial y} = 0\,, \tag{10}$$

$$u\frac{\partial u}{\partial x} + v\frac{\partial u}{\partial y} - F = \frac{1}{Re_0}\frac{\partial^2 u}{\partial y^2} - (bu + cu^2)\,, \tag{11}$$

$$u\frac{\partial \theta}{\partial x} + v\frac{\partial \theta}{\partial y} = \frac{1}{Re_0\,Pr}\frac{\partial^2 \theta}{\partial y^2} + \frac{1}{Re_0\,Pr}k\,(\theta_\mathrm{s} - \theta)\,, \tag{12}$$

$$\frac{\partial^2 \theta_\mathrm{s}}{\partial y^2} - k_\mathrm{s}\,(\theta_\mathrm{s} - \theta) = 0\,, \tag{13}$$

with

$$b = \frac{128}{\pi Re_0}\frac{1-\phi}{\phi}\,, \qquad c = \frac{1}{\pi}\frac{2(1-\phi) + 12.8(1-\phi)^2}{\phi}\,. \tag{14}$$

and

$$k = \frac{4(1-\phi)}{\phi}\,Nu_\mathrm{c}\,, \qquad k_\mathrm{s} = 4\frac{\hat{\kappa}}{\hat{\kappa}_\mathrm{s}}\,Nu_\mathrm{c}\,. \tag{15}$$

For the derivation of equations (10)–(13) we have used the fact that the porosity ϕ is constant and that the flow evolves in the positive x direction, i.e. $u > 0$. Also, in the momentum equation (11), F is the only non-vanishing term of the pressure gradient $\nabla\hat{p}$ and represents the external pressure forcing required to sustain the flow inside the porous medium. Therefore, this term is strictly positive, $F > 0$. Herein, the forcing F is assumed to be constant. Finally, the boundary conditions for the system (10)–(11) read,

$$u(0,y) = 1\,, \quad v(0,y) = 0\,, \quad \theta(0,y) = 0\,, \quad \theta_\mathrm{s}(0,y) = 0\,, \tag{16}$$

$$u(x,0) = 0\,, \quad v(x,0) = 0\,, \quad \theta(x,0) = 1\,, \quad \theta_\mathrm{s}(x,0) = 1\,. \tag{17}$$

3 Free-stream conditions

With regard to the free stream outside the boundary layer, the temperatures of both the solid matrix and the fluid are equal to that of the incoming stream, $\theta_\mathrm{s} = \theta = 0$. Also, in the free stream, the horizontal velocity does not vary in the vertical direction and, therefore,

$$\lim_{y\to\infty}\frac{\partial u}{\partial y} = 0\,, \qquad \lim_{y\to\infty}\frac{\partial^2 u}{\partial y^2} = 0\,. \tag{18}$$

The free-stream velocity inside the porous medium is denoted by u_e. By inserting relations (18) in the momentum equation (11), we obtain the

following equation for u_e,

$$u_\mathrm{e}\frac{\mathrm{d}u_\mathrm{e}}{\mathrm{d}x} \;=\; F-(bu_\mathrm{e}+cu_\mathrm{e}^2)\,. \tag{19}$$

For fixed porosity ϕ, the parameters b and c are constant and, therefore, (19) is a Riccati equation. This equation can be integrated analytically [16], resulting in a transcendental equation for u_e. It can also be integrated numerically, e.g. via a Runge-Kutta method. Therefore, in the computation of boundary-layer profiles, u_e is calculated beforehand.

It is also noted that, as $x\to\infty$, u_e converges to a terminal velocity u_∞,

$$u_\infty \;=\; \frac{-b+\sqrt{b^2+4cF}}{2c} \;<\; 1\,. \tag{20}$$

In other words, u_∞ is the Darcy-Forchheimer velocity, i.e. the fluid velocity for steady flow in porous media according to the Darcy-Forchheimer law. For fixed ϕ and Re_0, there is a unique correspondence between the terminal velocity u_∞ and the forcing F. In the present study we have assumed that $F<b+c$, which implies that u_e decreases monotonically from $u_\mathrm{e}=1$ at $x=0$ to $u_\mathrm{e}=u_\infty$ at $x\to\infty$. Nonetheless, one can also consider flows with F being large enough so that u_∞ is higher than unity.

4 Transformation of the boundary-layer equations

First we introduce the stream function Ψ so that the continuity equation (10) is automatically satisfied, $u=\frac{\partial\Psi}{\partial y}$ and $v=-\frac{\partial\Psi}{\partial x}$. Then we apply the so-called Görtler transformation [28, 29] which is essentially a change of variables from (x,y) to (ξ,η),

$$\xi \;:=\; \int_0^x u_\mathrm{e}(\bar{x})\,\mathrm{d}\bar{x}\,, \qquad \eta \;:=\; u_\mathrm{e}y\sqrt{\frac{Re_0}{2\xi}}\,. \tag{21}$$

According to this transformation, ξ is related to x. Whereas η is related to both x and y and plays a role analogous to that of the similarity variable in self-similar boundary layers. Also, without loss of generality, we can write the stream function in the following form,

$$\Psi \;=\; \sqrt{\frac{2\xi}{Re_0}}\,f(\xi,\eta)\,. \tag{22}$$

Next we introduce the following notation. Differentiation with respect to x or η is denoted by the prime symbol, $u_\mathrm{e}'=\frac{\mathrm{d}u_\mathrm{e}}{\mathrm{d}x}$, $f'=\frac{\partial f}{\partial\eta}$ and so on and so forth.

Whereas differentiation with respect to ξ is denoted by $\frac{\partial}{\partial \xi}$. Then, the velocity components u and v are cast as follows,

$$u \;=\; u_{\mathrm{e}} f' \,, \tag{23}$$

and

$$v \;=\; -\sqrt{\frac{2\xi}{Re_0}} \left(\frac{\eta u_{\mathrm{e}}'}{u_{\mathrm{e}}} - \frac{\eta u_{\mathrm{e}}}{2\xi} \right) f' - \left(\frac{f}{\sqrt{2\xi Re_0}} + \sqrt{\frac{2\xi}{Re_0}} \frac{\partial f}{\partial \xi} \right) u_{\mathrm{e}} \,. \tag{24}$$

By applying the change of variables (21) and (22), the governing equations (11)–(13) are transformed to the following system for f, θ and θ_{s},

$$(f''' + f f'') + 2\xi \left(f'' \frac{\partial f}{\partial \xi} - f' \frac{\partial f'}{\partial \xi} \right) + \beta_1 \left(1 - f'^2 \right) + \beta_2 \left(1 - f' \right) \;=\; 0 \,, \tag{25}$$

$$\frac{1}{Pr} \theta'' + \left(f + 2\xi \frac{\partial f}{\partial \xi} \right) \theta' - 2\xi f' \frac{\partial \theta}{\partial \xi} + \frac{2h\xi}{u_{\mathrm{e}}^2} \left(\theta_{\mathrm{s}} - \theta \right) \;=\; 0 \,, \tag{26}$$

$$\theta_{\mathrm{s}}'' - \frac{2\xi k_{\mathrm{s}}}{Re_0 u_{\mathrm{e}}^2} \left(\theta_{\mathrm{s}} - \theta \right) \;=\; 0 \,, \tag{27}$$

with

$$\beta_1(\xi) \;=\; \frac{2\xi \left(u_{\mathrm{e}}' + c \right)}{u_{\mathrm{e}}^2} \,, \qquad \beta_2(\xi) \;=\; \frac{2\xi b}{u_{\mathrm{e}}^2} \,. \tag{28}$$

Also, by using the change of variables (21), the boundary conditions (16) and (17) are transformed as follows,

$$f(\xi, 0) \;=\; 0 \,, \qquad f'(\xi, 0) \;=\; 0 \,, \qquad \theta(\xi, 0) \;=\; 1 \,, \qquad \theta_{\mathrm{s}}(\xi, 0) \;=\; 1 \,. \tag{29}$$

These are supplemented with the following free-steam conditions,

$$f'(\xi, \infty) \;=\; 1 \,, \qquad \theta(\xi, \infty) \;=\; 0 \,, \qquad \theta_{\mathrm{s}}(\xi, \infty) \;=\; 0 \,. \tag{30}$$

The last relations imply that as $\eta \to \infty$, the velocity becomes equal to the free-stream velocity u_{e} and that the temperatures of both phases become equal to that of the incoming stream.

5 Solution method

The transformed equations (25)–(27) are solved numerically via the local non-similarity solution method [9, 17]. Its main advantages are conceptual simplicity and ease of implementation. Over the years, it has been used in several numerical studies of both hydrodynamic and thermal boundary layers. It is worth adding that the developers of this method [9] reported good agreement between its predictions and those of finite-difference methods for a series of

nonsimilar boundary layers in pure-fluid domains, such as Howarth's retarded flow, cylinder in cross flow and flat plate with mass injection. Moreover, in their study of flow over a wedge embedded in a porous domain, the authors of [10] reported good agreement between the predictions of local nonsimilarity, finite difference and series expansion methods.

The local nonsimilarity method is based on the premise that since the variations of the various variables are much larger in the cross-stream direction y than in the streamwise direction x, then it is expected that the derivatives of f and θ with respect to η are considerably larger than those with respect to ξ. One can then take advantage of this property and approximate the partial differential equations (25)–(27) by a truncated series of ODEs.

According to this method, for the momentum equation (25), we define,

$$g := \frac{\partial f}{\partial \xi}, \tag{31}$$

which is treated as a new unknown variable. Then we differentiate (25) with respect to ξ to obtain an equation in terms of g. In this new equation, terms containing derivatives with respect to ξ are ignored. Whereas all terms of (25) are retained. The boundary conditions (29) and (30) for f are also differentiated with respect to ξ so as to obtain boundary conditions for g. This process leads to the following system of ODEs with η being the independent variable,

$$\begin{cases} f''' + ff'' + 2\xi\left(f''g - f'g'\right) + \beta_1\left(1 - f'^2\right) + \beta_2\left(1 - f'\right) = 0, & (32) \\ \\ g''' + fg'' - 2\left(\beta_1 + 1\right)f'g' - \beta_2 g' + 3f''g + \dfrac{\mathrm{d}\beta_1}{\mathrm{d}\xi}\left(1 - f'^2\right) + \\ \dfrac{\mathrm{d}\beta_2}{\mathrm{d}\xi}\left(1 - f'\right) = 0. & (33) \end{cases}$$

with boundary conditions,

$$f(\xi, 0) = g(\xi, 0) = 0, \qquad f'(\xi, 0) = g'(\xi, 0) = 0, \tag{34}$$

$$f'(\xi, \infty) = 1, \qquad g'(\xi, \infty) = 0. \tag{35}$$

For the energy equation (26) we follow the same procedure and define,

$$\varphi := \frac{\partial \theta}{\partial \xi}, \tag{36}$$

which is also treated as an unknown variable. We then differentiate (26) with respect to ξ and obtain an equation in which we ignore terms that contain derivatives with respect to ξ. Nonetheless, all terms of (26) are retained. We also differentiate the boundary conditions (29) and (30) for θ to get conditions

for φ. This leads to the following system of ODEs with respect to η,

$$\begin{cases} \dfrac{1}{Pr}\theta'' + (f + 2\xi g)\theta' - 2\xi f'\varphi - \dfrac{2h\xi}{u_e^2}(\theta_s - \theta) = 0\,, & (37) \\ \dfrac{1}{Pr}\varphi'' + (f + 2\xi g)\varphi' - 2(f' + \xi g')\varphi - 3g\theta' + \dfrac{2h}{u_e^2}(\theta_s - \theta) = 0\,, & (38) \\ \theta_s'' - \dfrac{2\xi k_s}{Re_0 u_e^2}(\theta_s - \theta) = 0\,, & (39) \end{cases}$$

with boundary conditions,

$$\theta(\xi, 0) = 1\,, \qquad \theta_s(\xi, 0) = 1\,, \qquad \varphi(\xi, 0) = 0 \tag{40}$$

$$\theta(\xi, \infty) = 0\,, \qquad \theta_s(\xi, \infty) = 0\,, \qquad \varphi(\xi, \infty) = 0\,. \tag{41}$$

The energy equation for the solid phase (27) has not been truncated because it does not involve derivatives with respect to ξ. In fact, the boundary layers for θ_s are nonsimilar by virtue of the presence of θ in the source term of (27).

Since the solutions for the hydrodynamic boundary layer do not depend on θ or θ_s, then we first solve the system (32)–(33) at the desired streamwise locations x. In our study this is achieved via simple shooting. During each iteration step of the shooting method, the ODEs (32)–(33) are integrated via a 4th-order Runge-Kutta scheme with an error tolerance of $\epsilon_0 = 10^{-7}$. The upper bound of the integration $\eta_{\max}$ is determined via the approach proposed in [9]. According to it, $\eta_{\max}$ is initially assigned a small value so that simple shooting can easily yield a converged solution. Then, its value is progressively increased until the pre-assigned tolerances on the computation of the dependent variables are satisfied. In this particular case, on the basis of the second of relations (18) we readily infer that $\lim_{\eta\to\infty} f''(\xi, \eta) = 0$. Therefore, $\eta_{\max}$ is considered to be sufficiently large when the finite-difference approximation of $f''(\eta_{\max})$ becomes smaller than a pre-assigned tolerance ϵ_2. In our study, we have set $\epsilon_2 = 10^{-5}$. Also, for a given $\eta_{\max}$, the shooting method is assumed to have converged when the values of $f'(\eta_{\max})$ and $g'(\eta_{\max})$ differ from the boundary values (35) by less than $\epsilon_1 = 10^{-5}$.

With regard to the system (37)–(39), numerical tests conducted in the context of this study, showed that the simultaneous integration of these equations via simple shooting is not always stable. For this reason, we have employed an outer iterative procedure that involves sequential numerical integration of these equations based on the last available estimates. For example, the $(i+1)$-th estimate of φ, φ^{i+1}, is computed by integrating (38) and using the last available estimates, θ^i and θ_s^i. In an analogous manner, equations (37) and (39) are integrated to obtain the next estimates, θ^{i+1} and θ_s^{i+1} respectively. This iterative procedure is assumed to have converged when the difference between the l^2 norm of two successive estimates for each dependent variable (θ, θ_s and

φ) falls below a pre-determined tolerance ϵ_2. In our computations, we have used the tolerance value, $\epsilon_3 = 5 \times 10^{-4}$.

In summary, the numerical procedure involves four tolerances: ϵ_0 is the tolerance in the numerical integration of the ODEs, ϵ_1 is the tolerance of the simple shooting method for the systems (32)–(33) and (37)–(39), whereas ϵ_2 relates to the truncation of the computational domain in the η direction. Finally, ϵ_3 is the convergence tolerance for the outer iterative procedure for system (37)–(39). Therefore, the accuracy bound in the computation of θ and θ_s is set by ϵ_3.

This outer iterative procedure for the system (37)–(39) requires two sets of initial estimates. In the first set, the estimates of all dependent variables are set equal to zero. In the second set, at each solution point η, the estimate for φ is set to the tolerance ϵ_2. Whereas the second set of estimates for θ and θ_s are computed by solving numerically (26)–(27) via the local similarity method. According to it, derivatives with respect of ξ are ignored in (26). This amounts to a system consisting of equation (37) in which we set $\varphi = 0$ and of equation (39). This system is solved simultaneously via simple shooting in a similar manner to that for the integration of (32)–(33). The advantages of computing initial estimates for θ and θ_s by solving (26)–(27) via the local similarity method are twofold. Firstly, these estimates are not too far from the actual solution and, secondly, this procedure provides an estimation of the thicknesses of the thermal boundary layers. This is important because, as it will be shown in the results section, the thicknesses of the thermal layers can be substantially different than that of the corresponding hydrodynamic layer. Finally, it may be added that the shooting-splitting method [30] could be an alternative to the outer iterative procedure for the system (37)–(39). Nonetheless, this option was not pursued in the present work since the outer iterative procedure was straightforward to implement and did not cause any stability issues.

The numerical method for the computation of the boundary-layer profiles is provided in the form of pseudo-code in Algorithm 1. Therein $\mathcal{S}_f$, $\mathcal{S}_\varphi$, $\mathcal{S}_\theta$ and $\mathcal{S}_{\theta_s}$ are, respectively, the solution operators for (32)–(33), (38), (37) and (39), based on simple shooting. Whereas $\mathcal{S}_{ss}$ is the local-similarity solution operator for (26)–(27) and is also based on simple shooting.

6 Numerical results

In this section we present numerical results for the boundary layers of two different fluids. In all cases presented herein, the porosity of the medium is set at $\phi = 0.95$, the free-stream Reynolds number based on the cylinder diameter is $Re_0 = 50$, and the external forcing F is set to a value such that the terminal free-stream velocity is $u_\infty = 0.25$.

For these parameters, the variation of the free-stream velocity u_e with x is plotted in figure 2a. We observe that close to the edge of the flat plate u_e decreases rapidly. However, further downstream it decreases at a lower rate

Algorithm 1 Integration of the boundary-value problem (32)–(41).

For a large set of values of x, integrate (19) to compute u_{e}.

For a given x, integrate (21) to compute ξ.

For a given $\eta_{\max}$ solve (32)–(33): $\mathcal{S}_f(f, g;\ \eta_{\max}) = 0$.

if $f''(\eta_{\max}) > \epsilon_2$ **then**

Increase $\eta_{\max}$ and repeat the previous step.

end if

Initialize: $\theta^0 = 0,\ \theta_{\mathrm{s}}^0 = 0,\ \varphi^0 = 0\ \ \varphi^1 = \epsilon_3$.

Solve (26)–(27) via the local similarity method: $\mathcal{S}_{ss}(\theta^1, \theta_{\mathrm{s}}^1;\ \eta_{\max}) = 0$.

if $|\theta_{\mathrm{s}}^{1\prime}(\eta_{\max})| > \epsilon_2$ **then**

Increase $\eta_{\max}$ and repeat previous step.

end if

while $\frac{\|\theta^i\| - \|\theta^{i-1}\|}{\|\theta^i\|}$ or $\frac{\|\theta_{\mathrm{s}}^i\| - \|\theta_{\mathrm{s}}^{i-1}\|}{\|\theta_{\mathrm{s}}^i\|}$ or $\frac{\|\varphi^i\| - \|\varphi^{i-1}\|}{\|\varphi^i\|} > \epsilon_3$ **do**

Solve (38) for φ^{i+1}: $\mathcal{S}_\varphi(\theta^i, \theta_{\mathrm{s}}^i, \varphi^{i+1};\ \eta_{\max}) = 0$.

Solve (37) for θ^{i+1}: $\mathcal{S}_\theta(\theta^{i+1}, \theta_{\mathrm{s}}^i, \varphi^{i+1};\ \eta_{\max}) = 0$.

Solve (39) θ^{i+1}: $\mathcal{S}_{\theta_{\mathrm{s}}}(\theta^{i+1}, \theta_{\mathrm{s}}^{i+1}, \varphi^{i+1};\ \eta_{\max}) = 0$.

$i \leftarrow i + 1$.

end while

if $|\theta_{\mathrm{s}}'(\eta_{\max})| > \epsilon_2$ **then**

Increase $\eta_{\max}$ and repeat the previous loop.

end if

and attains its terminal value u_∞ at a large distance from the edge. The plot of the thickness of the hydrodynamic boundary layer δ is presented in figure 2b. Overall, δ is quite small and equal to a few cylinder diameters. It is interesting to observe that δ exhibits an overshoot. More specifically, it increases rapidly close to the edge, reaches a peak and then decreases slowly to a terminal value. This feature is quite unusual because, in most flows, the thicknesses of hydrodynamic boundary layers increase monotonically with the streamwise distance. This feature has been analyzed in detail in [16] and occurs when the external pressure forcing F is sufficiently small so that u_{e} decays fast enough for the parameter β_1 to change sign at some distance.

Velocity profiles at different distances from the edge of the flat plate are plotted in figure 3. From these plots we reaffirm that the fluid velocity increases rapidly with y and attains the free-stream value at a few unit lengths above the flat plate. Once u_{e} reaches its terminal value, i.e. once $u_{\mathrm{e}} \approx u_\infty$ which in

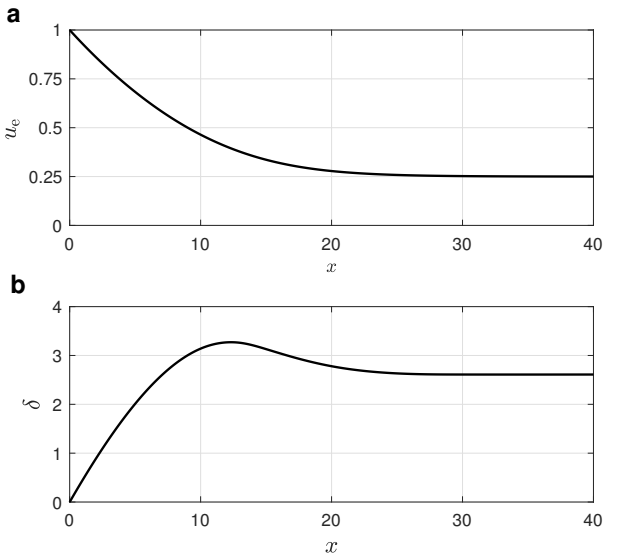


Fig. 2 (a) Plot of the free-stream velocity u_e inside a porous medium above a flat plate. (b) Thickness of the hydrodynamic boundary layer δ. The parameters are as follows, $\phi = 0.95$, $Re_0 = 50$ and $u_\infty = 0.25$.

this case occurs at $x \approx 30$, then the velocity profile stabilizes and no longer evolves with the streamwise distance x.

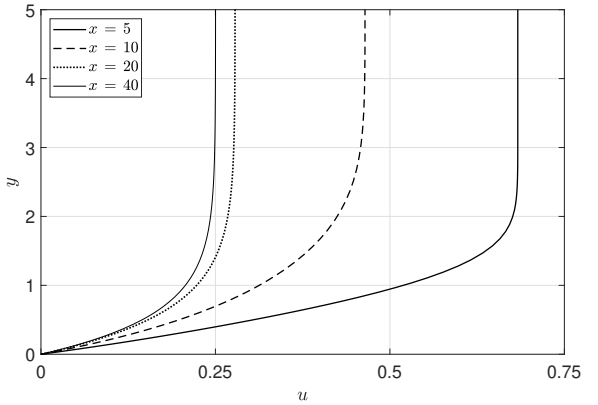


Fig. 3 Fluid velocity profiles at different distances from the edge of the flat plate. $\phi = 0.95$, $Re_0 = 50$ and $u_\infty = 0.25$.

In the following subsections we turn our attention to the structure of the thermal boundary layers for the problem in hand. As mentioned above, we present results for two different cases. In the first one the working fluid is air

at $Pr = 0.73$ while in the second one it is liquid water at $Pr = 7$. In both cases, the fibers of the solid matrix are supposed to be made of cast iron.

6.1 Forced convection of air

The thermal conductivity of air at room temperature is $\hat{k} \approx 0.026$ W/(m K) while that of the solid material is $\hat{k}_{\rm s} \approx 52$ W/(m K). Due to the high conductivity ratio, the heat flux in the solid matrix is much higher than in the fluid. This in turn implies that the flat plate exchanges heat with the solid matrix at a much higher rate than with the fluid. Therefore, $\theta_{\rm s}$ is expected to be higher than θ.

This is indeed corroborated by the plots of the temperature profiles that are shown in figure 4. More specifically, in this figure we show profiles for both θ and $\theta_{\rm s}$ at different distances from the edge of the flat plate. We observe that, close to the edge, the thermal non-equilibrium between the two phases is very high and θ decreases at a much higher rate than $\theta_{\rm s}$. At larger distances, the difference between the temperatures of the two phases is getting smaller; nonetheless, $\theta_{\rm s}$ remains uniformly higher than θ.

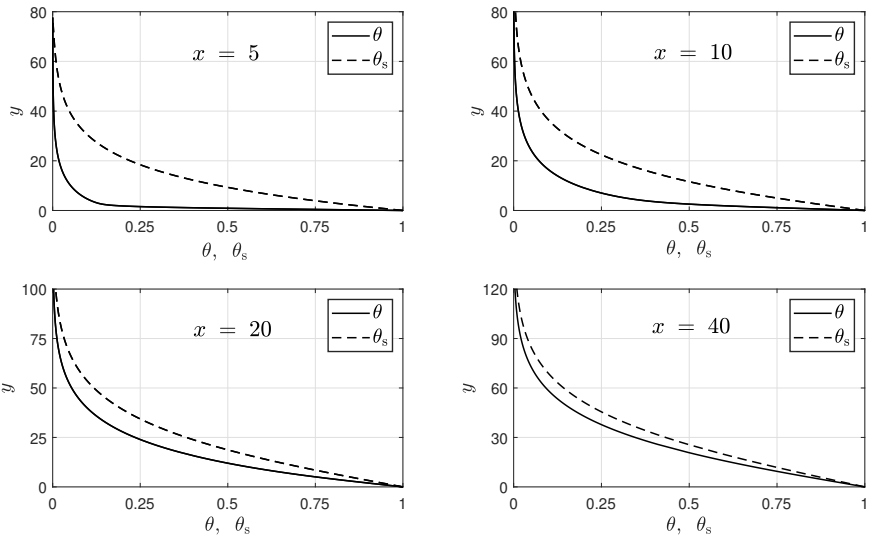


Fig. 4 Forced convection of air at $Pr = 0.73$. Profiles of the normalized temperatures of the two phases, θ and $\theta_{\rm s}$ respectively, at different distances from the edge of the flat plate.

Another interesting observation from figure 4 is that both θ and $\theta_{\rm s}$ approach their free-stream value of zero quite slowly and at a much lower rate than the velocity u approaches $u_{\rm e}$. This in turn implies that the thermal boundary layers are much thicker than the hydrodynamic one. In figure 5 we present plots of the thicknesses of the thermal layers of the fluid and solid matrix, δ_θ and $\delta_{\theta_{\rm s}}$ respectively, which confirm this assessment. Herein δ_θ (equivalently,

δ_{θ_s}) is defined as the vertical distance at which θ (equivalently, θ_s) becomes equal to 0.01. In the plots of figure 5 we observe that δ_θ and δ_{θ_s} are one to two orders of magnitude higher than δ. For example, at $x = 40$, $\delta_\theta = 103.6$ and $\delta_{\theta_s} = 118.3$ whereas $\delta = 2.6$.

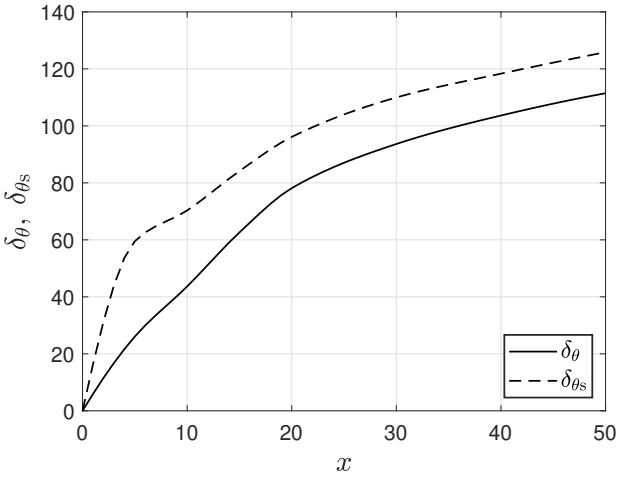


Fig. 5 Forced convection of air at $Pr = 0.73$. Profiles of the thermal boundary-layer thicknesses of the fluid phase and solid matrix, δ_θ and δ_{θ_s} respectively.

It is worth noting that even though the hydrodynamic boundary layer is much thinner than the thermal ones, it would be inaccurate for the purposes of thermal analysis to assume that its thickness is negligible as in [11]. In fact, this would amount to assume that the flow is inviscid, i.e. $u = u_e$ and $v = 0$. In this case, the second term on the left-hand side of (26) would vanish. This, in turn, would result in different values of θ' and θ'_s at the wall hence different heat fluxes and different temperature profiles.

In figure 5 we can also observe that both δ_θ and δ_{θ_s} increase monotonically with x. In other words, contrary to the thickness of the hydrodynamic layer, δ_θ and δ_{θ_s} do not exhibit an overshoot. Close to the edge of the flat plate, they increase quite rapidly, as expected. However, at larger distances, they increase at a lower rate. We also observe that whereas δ becomes constant once u_e reaches its terminal value u_∞, both δ_θ and δ_{θ_s} keep increasing even at large distances from the edge.

Another important feature is that the thermal layer of the solid matrix is quite thicker than that of the fluid. For example, at $x = 5$, the difference $\delta_{\theta_s} - \delta_\theta$ becomes higher than 30 unit lengths. This is due to the large thermal nonequilibriium between the two phases, especially close to the edge, which is attributed to the high conductivity ratio. Nonetheless, $\delta_{\theta_s} - \delta_\theta$ decreases with distance albeit rather slowly. For example, at $x = 50$ it has been reduced to 14 unit lengths.

As is customary, the local heat transfer between the flat plate and the fluid, $\hat{q}_{\rm w}$, is written as the product between a local heat-transfer parameter, $\hat{h}_{\rm w}$, and the temperature difference between the free stream and the flat plate, i.e.

$$\hat{q}_{\rm w} \;=\; -\hat{k}\left(\frac{\partial \hat{T}}{\partial \hat{y}}\right)_{\hat{y}=0} \;=\; \hat{h}_{\rm w}\left(\hat{T}_{\rm w}-\hat{T}_0\right). \tag{42}$$

The local heat-transfer parameter can be expressed in terms of the local Nusselt number which is defined as $Nu_x = \frac{\hat{h}_{\rm w}\hat{x}}{\hat{k}}$. Upon non-dimensionalization, equation (42) yields the following relation between Nu_x and the local free-stream Reynolds number, $Re_x = \frac{\hat{u_{\rm e}}\hat{x}}{\hat{\nu}}$,

$$\frac{Nu_x}{\sqrt{Re_x}} \;=\; -\theta'(\xi,0)\sqrt{\frac{u_{\rm e}x}{2\xi}}\,. \tag{43}$$

The same procedure can be followed for the local heat transfer between the flat plate and the solid matrix, $\hat{q}_{\rm ws}$. More specifically, we can set,

$$\hat{q}_{\rm ws} \;=\; -\hat{k}_{\rm s}\left(\frac{\partial \hat{T}_{\rm s}}{\partial \hat{y}}\right)_{\hat{y}=0} \;=\; \hat{h}_{\rm ws}\left(\hat{T}_{\rm w}-\hat{T}_0\right), \tag{44}$$

and define $Nu_{x_{\rm s}} = \frac{\hat{h}_{\rm ws}\hat{x}}{\hat{k}_{\rm s}}$. Then, upon non-dimensionalization of (44), we obtain,

$$\frac{Nu_{x_{\rm s}}}{\sqrt{Re_x}} \;=\; -\theta'_{\rm s}(\xi,0)\sqrt{\frac{u_{\rm e}x}{2\xi}}\,. \tag{45}$$

In figure 6 we provide the profiles for both $\frac{Nu_x}{\sqrt{Re_x}}$ and $\frac{Nu_{x_{\rm s}}}{\sqrt{Re_x}}$. According to them, these two quantities follow different trends. In particular, $\frac{Nu_x}{\sqrt{Re_x}}$ is quite high close to the edge but decreases rapidly with x and eventually reaches its asymptotic value far downstream. In other words, Nu_x becomes proportional to $\sqrt{Re_x}$ only at large distances from the edge of the flat plate. This is evidently due to the fact that the hydrodynamic and thermal boundary layers of the flow interest are nonsimilar. On the contrary, in laminar convection in a pure-fluid domain, Nu_x is everywhere proportional to $\sqrt{Re_x}$ [27]. We further observe that $\frac{Nu_{x_{\rm s}}}{\sqrt{Re_x}}$ follows the opposite trend. It attains small values close to the edge and increases very slowly with x until it reaches its asymptotic value. It is also interesting to observe that Nu_x is always larger than $Nu_{x_{\rm s}}$. However the difference $Nu_x - Nu_{x_{\rm s}}$ (or, equivalently, the difference $\theta'(\xi,0) - \theta'_{\rm s}(\xi,0)$) decreases monotonically with x. This is due to the thermal non-equilibrium between the two phases which exhibits the same behavior, namely, it is high close to the edge but decreases with x.

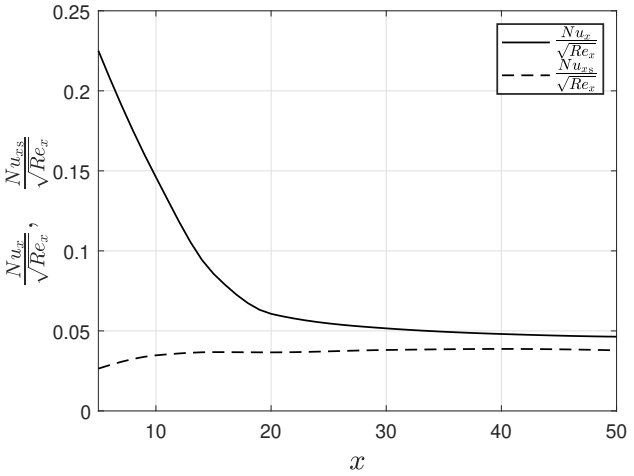


Fig. 6 Forced convection of air at $Pr = 0.73$. Profiles of the local Nusselt numbers of the fluid phase and solid matrix, Nu_x and $Nu_{x\mathrm{s}}$, respectively.

6.2 Forced convection of liquid water

Next we consider forced convection of liquid water at room temperature and $Pr = 7$. As in the previous case, the solid matrix is assumed to consist of cylinders made of cast iron (suitably coated so as to avoid rust). The thermal conductivity of liquid water at room temperature is $\hat{k} \approx 0.6$ W/(m K), which is still quite smaller than that of the solid material, $\hat{k}_\mathrm{s} \approx 52$ W/(m K).

In figure 7 we present profiles of the normalized temperatures of the two phases θ and θ_s at different distances from the edge of the flat plate. These profiles share some properties with the corresponding ones of the previous case at lower Prandtl number. In particular, θ_s is uniformly higher than θ, which is attributed to the fact that $\hat{k}_\mathrm{s}$ is much higher than $\hat{k}$. Also, similarly to the previous case, the difference between the temperatures of the two phases, $\theta_\mathrm{s} - \theta$, is quite high at short distances from the edge but decreases with the streamwise distance. On the other hand, a marked difference with the previous case is that the temperatures converge to the free-stream value at a much higher rate. This is a direct consequence of the increase of the Prandtl number.

The thicknesses of the thermal boundary layers of the two phases are plotted in figure 8. The most striking feature is that they are smaller than the corresponding ones of the previous case by one order of magnitude. In other words, one order of magnitude increase of Pr results in one order of magnitude decrease of δ_θ and $\delta_{\theta_\mathrm{s}}$. It is also interesting to observe that even though Pr is much higher than unity, the thermal boundary layer of the fluid is still much thicker than the hydrodynamic one. This implies that the difference between the thicknesses of the thermal and hydrodynamic layers extends over a large range of Pr. As mentioned above, this difference can be traced to the high conductivity of the solid matrix which results in increased heat exchange

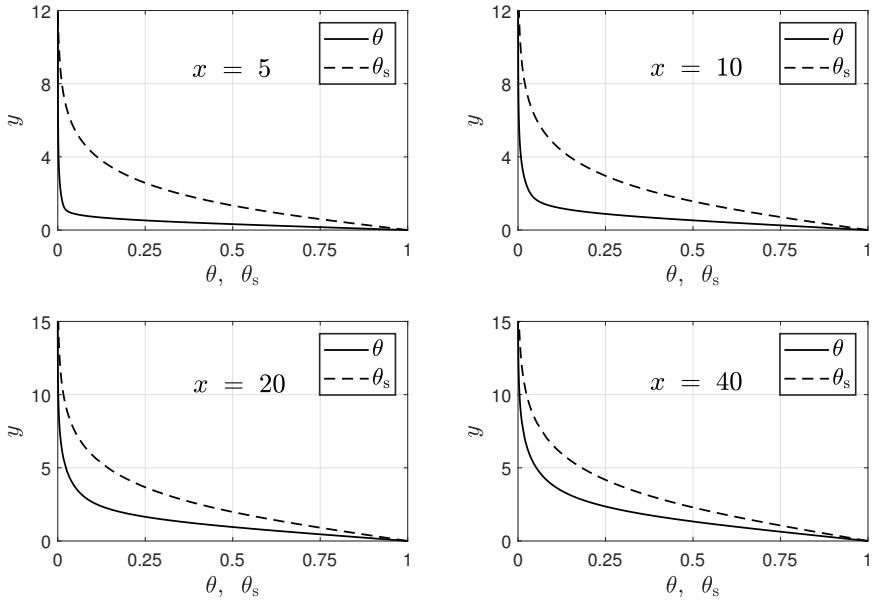


Fig. 7 Forced convection of liquid water at $Pr = 7$. Profiles of the normalized temperatures of the two phases, θ and θ_s respectively, at different distances from the edge of the flat plate.

between the flat plate and the matrix. This in turn reduces the amplitudes of the thermal gradients thereby increasing the thicknesses of the thermal layers.

Apart from the large difference in the amplitude, the profiles of δ_θ and δ_{θ_s} have certain common features with those in forced convection of air. For example, neither δ_θ nor δ_{θ_s} exhibit any overshoot but, instead, they increase monotonically with x. The increase rate is quite high close to the edge of the flat plate but becomes smaller at larger distances. Another common feature is that the difference between δ_{θ_s} and δ_θ becomes large close to the edge but is slowly reduced further downstream.

In figure 9 we present plots of the local Nusselt numbers for the case in hand. These plots are markedly different than those for air. In particular, the Nusselt numbers of both phases are considerably higher than before; for example, at large distances from the edge, they are 10 to 14 times higher. Another important difference is that $\frac{Nu_x}{\sqrt{Re_x}}$ increases with the streamwise distance (whereas in the case of air it decreases with it). Yet another difference is that the variation of both $\frac{Nu_x}{\sqrt{Re_x}}$ and $\frac{Nu_{xs}}{\sqrt{Re_x}}$ with x is much milder than in air. More specifically, both of these quantities increase slowly and appear to approach a constant value far downstream, i.e. the local Nusselt numbers become proportional to $\sqrt{Re_x}$. In this case however, this scaling is attained at much larger distances than in the previous case with air.

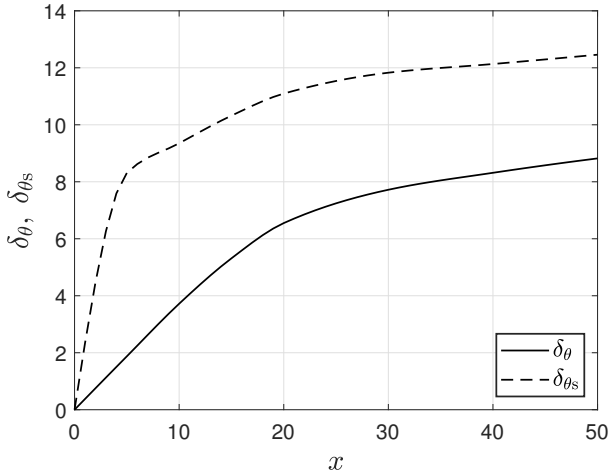


Fig. 8 Forced convection of liquid water at $Pr = 7$. Profiles of the thicknesses of the thermal boundary-layer thicknesses of the fluid phase and solid matrix, δ_θ and $\delta_{\theta_\mathrm{s}}$ respectively.

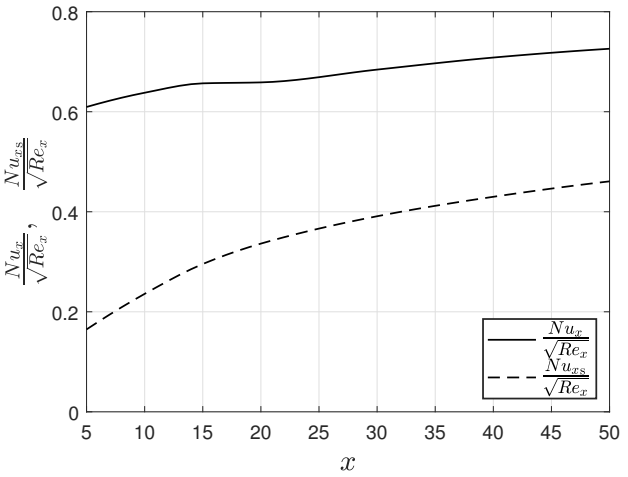


Fig. 9 Forced convection of liquid water at $Pr = 7$. Profiles of the local Nusselt numbers of the fluid phase and solid matrix, Nu_x and $Nu_{x\mathrm{s}}$ respectively.

7 On the validity of the Local Thermal Equilibrium assumption

As it was shown in the previous section, for steady flow in a porous medium situated above a heated (equivalently, cooled) flat plate, both the solid matrix and the working fluid are maintained at nonequilibrium thermodynamic states, due to the energy supply from (equivalently, towards) the flat plate. Such

steady nonequilibrium states are commonly referred to as *stationary states* [31, 32]. Evidently, in the flow of interest, the stationary states of the two phases are different due to the difference between their temperatures. Moreover, according to our computations, this difference is quite significant close to the flat plate (small y); this is especially so for short and moderate streamwise distances from the edge. Therefore, the LTE assumption is not valid for the flow in hand. More generally, for variable-temperature flows in porous media, one can formally arrive in the same conclusion upon inspection of the energy equations (3) and (4) of the fluid and solid matrix, respectively. For if the temperatures of the two phases were indeed equal, then the governing system (1)–(4) would become overdetermined and (3) and (4) could not be satisfied simultaneously.

Nonetheless it is interesting to examine whether the LTE assumption can provide a reasonable approximation for the boundary-layer flows of interest. According to [1], a common approach is to assume that the temperatures of the two phases are equal and add (3) and (4). To this end, let us call "local-equilibrium" temperature $\hat{T}_{\rm eq}$ the common temperature of the two phases under the LTE assumption. As proposed in [1], by setting $\hat{T}_{\rm eq} = \hat{T} = \hat{T}_{\rm s}$ and adding (3) and (4), we obtain a single energy equation that is applicable in the entire porous medium. Its non-dimensionalization results in the following equation for the normalized local-equilibrium temperature, $\theta_{\rm eq} = \frac{\hat{T}_{\rm eq}-\hat{T}_0}{\hat{T}_{\rm w}-\hat{T}_0}$,

$$u\frac{\partial\theta_{\rm eq}}{\partial x} + v\frac{\partial\theta_{\rm eq}}{\partial y} \;=\; \frac{1}{Re_0\, Pr_{\rm eff}}\frac{\partial^2\theta_{\rm eq}}{\partial y^2}\,, \tag{46}$$

In the above equation, $Pr_{\rm eff}$ is the effective Prandtl number for the entire porous medium,

$$Pr_{\rm eff} \;=\; Pr\,\frac{\phi\hat{k}}{\phi\hat{k} + (1-\phi)\hat{k}_{\rm s}}\,. \tag{47}$$

The thermal boundary-layer equation (46) can also be solved via the local nonsimilarity method of [9, 17]. More specifically, we can apply the coordinate transformation (21) and define $\varphi_{\rm eq} := \frac{\partial\theta_{\rm eq}}{\partial\xi}$, The resulting system of coupled equations for $\theta_{\rm eq}$ and $\varphi_{\rm eq}$ reads,

$$\begin{cases} \dfrac{1}{Pr_{\rm eff}}\theta''_{\rm eq} + (f+2\xi g)\theta'_{\rm eq} - 2\xi f'\varphi_{\rm eq} \;=\; 0\,, & (48)\\[2ex] \dfrac{1}{Pr_{\rm eff}}\varphi''_{\rm eq} + (f+2\xi g)\varphi'_{\rm eq} - 2(f'+\xi g')\varphi - 3g\theta'_{\rm eq} \;=\; 0\,, & (49) \end{cases}$$

with boundary conditions,

$$\theta_{\rm eq}(\xi,0) \;=\; 1\,, \qquad \varphi_{\rm eq}(\xi,0) \;=\; 0\,, \tag{50}$$

$$\theta_{\rm eq}(\xi,\infty) \;=\; 0\,, \qquad \varphi_{\rm eq}(\xi,\infty) \;=\; 0\,. \tag{51}$$

For the case of forced convection of air $Pr = 0.73$, profiles of θ_{eq} at $x = 5$ and $x = 40$ are presented in figure 10. Therein the profiles of θ_{eq} are juxtaposed with those of θ and θ_{s} that were obtained by considering thermal nonequilibrium. These plots reveal that the profiles of θ_{eq} lie between those of θ and θ_{s}, with the exception of the outer region of the thermal boundary layer where the normalized temperatures approach zero. In that region θ_{eq} becomes smaller than θ. More specifically, close to the wall, θ_{eq} is closer to θ_{s}. But as y increases, it progressively gets closer to the profile of θ and eventually it becomes smaller than it near the edge of the thermal layer. It is worth adding that the deviation of θ_{eq} from either θ or θ_{s} is much more pronounced at small x, i.e. at short distances from the edge of the flat plate. This is expected because thermal non-equilibrium between the two phases is more significant at small x.

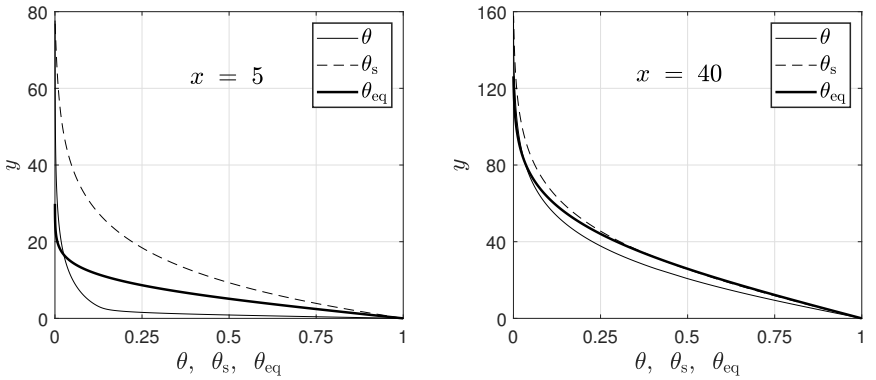


Fig. 10 Forced convection of air at $Pr = 0.73$. Profiles of the normalized local-equilibrium temperature θ_{eq} under the LTE assumption at two different distances from the edge (thick lines). For comparison purposes, the profiles of θ and θ_{s} are plotted well (fine lines).

For this case, i.e. convection of air at $Pr = 0.73$, the thickness $\delta_{\theta\mathrm{eq}}$ of the boundary layer of the local-equilibrium temperature is provided in figure 11. For comparison purposes, the plots of δ_{θ} and $\delta_{\theta_{\mathrm{s}}}$ have also been included in this figure. We observe that globally, $\delta_{\theta\mathrm{eq}}$ does not lie between δ_{θ} and $\delta_{\theta_{\mathrm{s}}}$ but is mildly lower than δ_{θ}. Moreover, the profile of $\delta_{\theta\mathrm{eq}}$ follows the same pattern as the profile of δ_{θ}. In particular, it grows at a similar rate close to the edge and also far downstream. For example, at $x = 50$, the value of $\delta_{\theta\mathrm{eq}}$ is approximately 95% of that of δ_{θ}. This indicates that even though the LTE assumption does not accurately predict the temperature profiles of the fluid at short and moderate distances from the edge, it nonetheless provides a reasonable approximation of the thickness of the thermal boundary layer of the fluid.

For completion purposes, we also present results for the case of forced convection of liquid water at $Pr = 7$. The profiles of θ_{eq} at $x = 5$ and $x = 40$ are shown in figure 12, together with the corresponding ones for θ and θ_{s}. As in the case of air, the profile of θ_{eq} lies in between those of θ and θ_{s}, except for the outer region of the boundary layer, i.e. the region where the

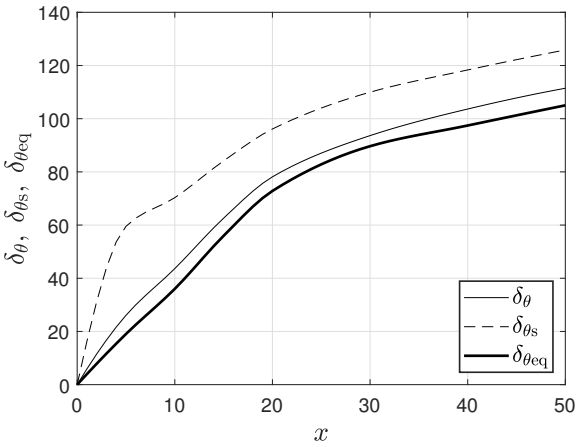


Fig. 11 Forced convection of air at $Pr = 0.73$. Profile of the thermal boundary-layer thickness $\delta_{\theta \mathrm{eq}}$ under the LTE assumption, (thick line). For comparison purposes, the profiles of δ_θ and $\delta_{\theta_\mathrm{s}}$ are plotted as well (fine lines).

normalized temperatures approach zero. In that region, θ_eq becomes smaller than θ. Also, the deviation of θ_eq from θ and θ_s is very pronounced at short distances from the edge of the flat plate but decreases with the streamwise distance, as does the thermal nonequilibrium between the two phases. Finally,

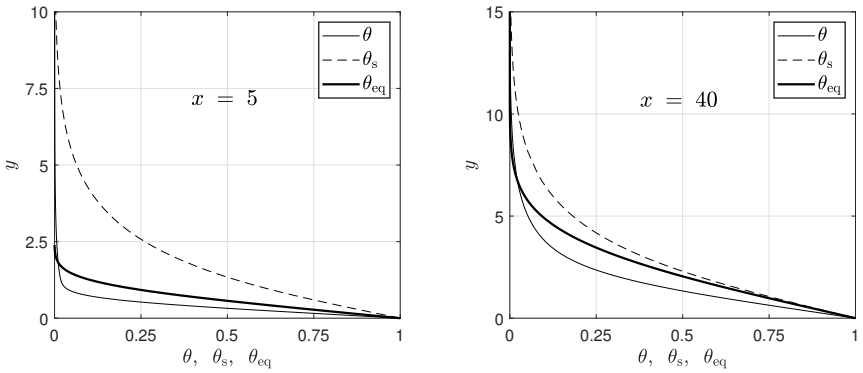


Fig. 12 Forced convection of liquid water at $Pr = 7$. Profiles of the normalized local-equilibrium temperature θ_eq under the LTE assumption at two different distances from the edge. For comparison purposes, the profiles of θ and θ_s are plotted as well (fine lines).

for water at $Pr = 7$, the thickness $\delta_{\theta \mathrm{eq}}$ of the boundary layer of the local-equilibrium temperature is plotted in figure 13. As before, the profile of $\delta_{\theta \mathrm{eq}}$ is quite similar to that of δ_θ albeit a little lower. For example, at large x, the value of $\delta_{\theta \mathrm{eq}}$ is approximately 90% of that of δ_θ. We can therefore assume that even at higher Prandtl numbers, the LTE assumption provides a reasonable

approximation of the thickness of the thermal boundary layer of the fluid at large distances from the leading edge.

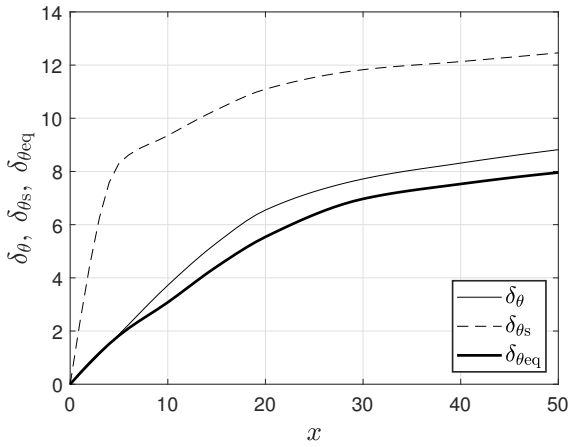


Fig. 13 Forced convection of liquid water at $Pr = 7$. Profile of the thermal boundary-layer thickness $\delta_{\theta \mathrm{eq}}$ under the LTE assumption, (thick line). For comparison purposes, the profiles of δ_θ and $\delta_{\theta_\mathrm{s}}$ are plotted as well (fine lines).

8 Conclusions

In this paper we have derived thermal boundary-layer solutions for forced convection of a fluid in a porous medium located above a flat plate. Additionally, we examined the structure of such thermal layers. An important aspect of our study is that it takes into account thermal nonequilibrium between the solid matrix and the fluid. The basic property of the boundary layers of interest is that they are nonsimilar. For this reason, the resulting boundary-layer equations were solved via the local nonsimilarity method, suitably adapted so as to account for the source terms representing interphasial heat exchange.

According to our computations, there are significant differences between the temperature distributions of the two phases. These differences are quite large at short and moderate distances from the edge of the flat plate but are slowly reduced at larger distances. Due to the presumed high conductivity ratio, the thermal boundary layer of the solid matrix is always thicker than that of the fluid. Also, the high conductivity of the solid enhances heat exchange with the flat plate hence interphasial heat exchange. As a result, the thermal boundary layers of both phases are considerably thicker than the hydrodynamic boundary layer, even at high Prandtl numbers. More specifically, for water at $Pr = 7$ the thermal boundary layers are 3 to 5 times thicker than the hydrodynamic one. Whereas for air at $Pr = 0.73$, they are 45 to 50 times thicker.

Our computations further showed that the scaling of the Nusselt number with the local free-stream Reynolds number $\sqrt{Re_x}$ is quite sensitive to the Prandtl number. For air at $Pr = 0.73$, the ratio $\frac{Nu_x}{\sqrt{Re_x}}$ decreases monotonically with distance but eventually reaches an asymptotic value far downstream. On the contrary, for $Pr = 7$ this ratio increases slowly with distance, until it reaches its asymptotic value. Nonetheless, far downstream, the local Nusselt number scales with the square root of the distance, independently of the Prandtl number.

Finally, we performed computations by invoking the local thermal equilibrium assumption. Our comparisons showed that this assumption results in significant errors in the temperature distribution of either phase, especially at short and moderate distances from the edge of the flat plate where thermal nonequilibrium is more pronounced. Nonetheless, it provides reasonable estimates for the thickness of the thermal boundary layer of the fluid phase.

- **Funding** No funding was received for conducting this study.
- **Conflict of interest** The author has no competing interests to declare that are relevant to the content of this article.

References

[1] Nield, D.A., Bejan, A.: Convection in Porous Media, 5th edn. Springer, New York (2017)

[2] Straughan, B.: Stability and Wave Motion in Porous Media. Springer, New York (2008)

[3] Vafai, C. (ed.): Handbook of Porous Media. CRC Press, Boca Raton, FL (2015)

[4] Das, M.K., Mukherjee, P.P., Muralidhar, K.: Modeling Transport Phenomena in Porous Media with Applications. Springer, Berlin (2018)

[5] Vafai, K., Tien, C.L.: Boundary and inertial effects on flow and heat transfer in porous media. Int. J. Heat Mass Tran. **24**, 195–203 (1981)

[6] Vafai, K., Thiyagaraja, R.: Analysis of flow and heat transfer at the interface region of a porous medium. Int. J. Heat Mass Tran. **2304**, 1391–1405 (1987)

[7] Beckermann, C., Viskanta, R.: Forced convection boundary layer flow and heat transfer along a flat plate embedded in a porous medium. Int. J. Heat Mass Tran. **30**, 1547–1551 (1987)

[8] Nakayama, A., Kokudai, T., Koyama, H.: Non-Darcian boundary layer flow and forced convective heat transfer over a flat plate in a fluid-saturated porous medium. J. Heat Tran. **112**, 157–162 (1990)

[9] Sparrow, E.M., Quack, H., Boerner, C.J.: Local nonsimilarity boundary-layer solutions. AIAA J. **8**, 1936–1942 (1970)

[10] Hossain, M.A., Banu, N., Nakayama, A.: Non-Darcy forced convection boundary layer flow over a wedge embedded in a saturated porous medium. Numer. Heat Tr. A - Appl. **26**, 399–414 (1994)

[11] Celli, M., Rees, D.A.S., Barletta, A.: The effect of local thermal non-equilibrium on forced convection boundary layer flow from a heated surface in porous media. Int. J. Heat Mass Tran. **53**, 3533–3539 (2010)

[12] Gogate, S.P., Bharati, M.C., Misbah, N.E., Kudenatti, R.B.: Forced convection boundary layer flow and heat transfer along a flat plate embedded in a porous medium. Arch. Appl. Mech. **93**, 551–569 (2023)

[13] Qawasmeh, B.R., Alrbrai, M., Al-Dahidi, S.: Forced convection heat transfer of Casson fluid in non-Darcy porous media. Int. Comm. Heat Mass **11**, 1–10 (2019)

[14] Farooq, U., Ijaz, M.A., Khan, M.I., Isa, S.S.P.M., Lu, D.C.: Modeling and non-similar analysis for Darcy-Forchheimer-Brinkman model of Casson fluid in a porous media. Int. Comm. Heat Mass **119**, 104955 (2020)

[15] Farooq, U., Hussain, M., Ijaz, M.A., Khan, W.A., Farooq, F.B.: Impact of non-similar modeling on Darcy-Forchheimer-Brinkman model for forced convection of Casson nano-fluid in non-Darcy porous media. Int. Comm. Heat Mass **125**, 105312 (2021)

[16] Papalexandris, M.V.: Boundary-layer flow in a porous domain above a flat plate. J. Eng. Math. **140**, 4 (2023)

[17] Sparrow, E.M., Yu, H.S.: Local nonsimilarity thermal boundary-layer solutions. ASME J. Heat Transfer **93**, 328–334 (1971)

[18] Papalexandris, M.V., Antoniadis, P.D.: A thermo-mechanical model for flows in superposed porous and fluid layers with interphasial heat and mass exchange. Int. J. Heat Mass Tran. **88**, 42–54 (2015)

[19] Antoniadis, P.D., Papalexandris, M.V.: Dynamics of shear layers at the interface of a highly porous medium and a pure fluid. Phys. Fluids **27**, 014104 (2015)

[20] Varsakelis, C., Papalexandris, M.V.: On the well-posedness of the Darcy-Brinkman-Forchheimer equations for coupled porous media-clear fluid flow. Nonlinearity **30**, 1449–1464 (2017)

[21] Papalexandris, M.V.: Attenuation of gaseous detonations by porous media

of fine microstructure. Combust. Flame **232**, 111518 (2021)

[22] Hamtiaux, V., Papalexandris, M.V.: Turbulent thermal convection in mixed porous-pure fluid domains. J. Fluid Mech. **961**, 27 (2023)

[23] Cowin, S.C.: Continuum Mechanics of Anisotropic Materials. Springer, New York (2013)

[24] Tanino, Y., Nepf, H.M.: Laboratory investigation of mean drag in a random array of rigid, emergent cylinders. J. Hydraul. Eng. **134**, 534–41 (2008)

[25] Sonnenwald, F., Stovin, V.R., Guymer, I.: Estimating drag coefficient for arrays of rigid cylinders representing emergent vegetation. J. Hydraul. Res. **57**, 591–597 (2019)

[26] Tinoco, R.O., Cowen, E.A.: The direct and indirect measurement of boundary stress and drag on individual and complex arrays of elements. Exp. Fluids **54**, 1–16 (2013)

[27] Incropera, F.P., DeWitt, D.P., Bergman, T.L., Lavine, A.S.: Fundamentals of Heat and Mass Transfer, 6th Edition. John Wiley, Hoboken, NJ (2007)

[28] Görtler, H.: A new series for the calculation of steady laminar boundary layers. J. Math. Mech. **6**, 1–66 (1957)

[29] Schlichting, H., Gersten, K.: Boundary-Layer Theory, 9th edn. Springer, Berlin (2017)

[30] Firnett, P.J., Troesch, B.A.: Shooting-splitting method for sensitive two-point boundary value problems. In: Bettis, D.G. (ed.) Proceedings of the Conference on the Numerical Solution of Ordinary Differential Equations, pp. 408–433. Springer, Berlin. Heidelberg (1974)

[31] Lebon, D.G., Jou, D., Casas-Vázquez, J.: Understanding Non-equilibrium Thermodynamics. Springer, Berlin (2008)

[32] De Groot, S.R., Mazur, P.: Non-equilibrium Thermodynamics. Dover Publications Inc., New York (2011)